CHEMISTRY OF MATERIALS

Article

pubs.acs.org/cm

Oxidative Etching and Metal Overgrowth of Gold Nanorods within Mesoporous Silica Shells

Tian-Song Deng,*[,†] Jessi E. S. van der Hoeven,[†] Anil O. Yalcin,[‡] Henny W. Zandbergen,[‡] Marijn A. van Huis,[†] and Alfons van Blaaderen*[,†]

[†]Soft Condensed Matter, Debye Institute for Nanomaterials Science, Utrecht University, Princetonplein 5, 3584 CC Utrecht, The Netherlands

[‡]Kavli Institute of Nanoscience, Delft University of Technology, Lorentzweg 1, 2628 CJ Delft, The Netherlands

Supporting Information

ABSTRACT: Composite noble metal-based nanorods for which the surface plasmon resonances can be tuned by composition and geometry are highly interesting for applications in biotechnology, imaging, sensing, optoelectronics, photovoltaics, and catalysis. Here, we present an approach for the oxidative etching and subsequent metal overgrowth of gold nanorods, all taking place while the nanorods are embedded in mesoporous SiO_2 shells (AuNRs@meso-SiO_2). Heating of the AuNRs@meso-SiO_2 in methanol with HCl resulted in reproducible oxidation of the AuNRs by dissolved O_2, specifically at the rod ends, enabling precise control over the aspect ratio of the rods. The etched-AuNRs@meso-SiO_2 were used as a template for the overgrowth of a second metal (Ag, Pd, and Pt), yielding bimetallic, core−shell structured nanorods. By varying the reaction rates of the metal deposition both smooth core−shell structures or gold nanorods covered with a dendritic overlayer could be made. This control over the morphology, including metal composition, and thus the plasmonic properties of the composite rods were measured experimentally and also confirmed by Finite-Difference Time-Domain (FDTD) calculations. The presented synthesis method gives great control over tuning over both plasmonic properties and the particle stability/affinity for specific applications.

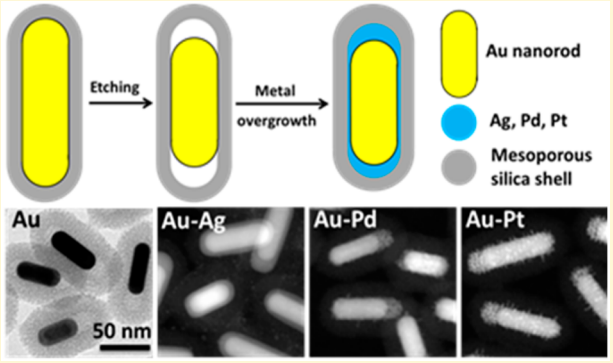

INTRODUCTION

Gold nanorods (AuNRs) possess two different surface plasmon resonances, one associated with a longitudinal and the other with a transverse mode of oscillations of the conduction electrons. The transverse surface plasmon resonance (TSPR) is in the visible spectrum with a wavelength around 510−540 nm, whereas the longitudinal surface plasmon resonance (LSPR) can be varied from the visible (~600 nm) to near-infrared wavelength range (>1200 nm), depending on the aspect ratio of the nanorod.[1−4] The tunable properties of the LSPR and the strong local electromagnetic field enhancements that can be realized close to the nanoparticle make AuNRs useful for a broad range of application fields that include sensing, such as in surface-enhanced Raman scattering (SERS)[5,6] or through changes in refractive index,[7] plasmon enhanced fluorescence,[8−10] optoelectronics,[11] data storage,[12] photothermal therapy,[13,14] (in vivo) imaging,[15−17] and biomedicine.[18,19] For the present work, it is important to mention that for the different applications, sometimes even opposite requirements are optimal with respect to the plasmonic properties of the particles. For instance, excessive damping of the plasmon resonance is detrimental for many applications in optoelectronics and plasmon field enhancement methodologies (such as in SERS and plasmon enhanced fluorescence), while the generation of heat out of plasmon induced by light absorption is what makes certain imaging[17] and medical applications[13,14] possible. For some applications, like catalysis and SERS, a rough metal interface is often measured or predicted to be advantageous. For other applications like in a femtosecond-light-pulse that induces a change in the aspect ratio of AuNRs which has been used in a data storage application,[12] a smooth defect free AuNR is optimal. For almost all applications, control over the actual position of the LSPR is important as well. For pure AuNRs, this tuning is possible through the aspect ratio. If composite particles, as studied in the present article, are an option, the composition in combination with the morphology provide an even wider spectrum of possibilities to tune the plasmonic properties.[20]

In principle, the aspect ratio of the AuNRs can be controlled during synthesis and/or via postselective-etching afterward. Presently, AuNRs are usually synthesized via a so-called seed-mediated growth method,[21−23] under the influence of the shape directing and stabilizing surfactant hexadecyltrimethylammonium bromide (CTAB) and shape inducing agent Ag, whereby

Received: September 24, 2015
Revised: September 30, 2015
Published: October 1, 2015

DOI: 10.1021/acs.chemmater.5b03749
Chem. Mater. 2015, 27, 7196−7203

the aspect ratio of the AuNRs can roughly be controlled by tuning the acidity of the growth solution. However, selective etching[24] after particle growth allows for more precise control of the aspect ratio. This has already been successfully shown for mild oxidation by cyanide,[25] Au(III),[26] O_2,[27] and H_2O_2.[28] The etching preferentially takes place at the ends of the nanorods,[26−28] leaving the diameter unchanged. Thus, the AuNRs are selectively shortened, enabling more precise control over the aspect ratio. So far, these etching processes were performed in AuNRs solutions with high CTAB concentrations as stability with metal particles is always an issue at higher ionic strengths because of the large Hamaker constants and thus van der Waals forces for these systems. However, the toxicity of CTAB is problematic when using bare AuNRs for in vivo studies.[18,19] Also in applications such as catalysis, the presence of a dense surfactant layer on the particles is undesirable, for it makes the Au metal surface inaccessible for reactants.[29] Therefore, a different stabilizing mechanism based on a nontoxic mesoporous silica layer[30,31] overcomes these problems with CTAB, as the silica coating significantly reduces the van der Waals forces, and is compatible with almost any solvent by surface modification, while keeping the AuNR accessible for surrounding molecules.[32] For example, Zhang et al.[15] demonstrated that multilayer-coated AuNRs (with a dyed SiO_2 shell and polymer layer) exhibited ultrahigh colloidal stability and excellent tunability, which makes them suitable for in vivo fluorescence imaging, SERS detection, and photothermic therapy. Apart from many developed coating schemes, an SiO_2 coating has also advantages in chemical and mechanical stabilities (including increased stability against temperature induced shape changes of AuNRs[32]), a tunable porosity, and optical transparency.[33,34] A thin SiO_2 shell also can act as a "spacer" to control the coupling distance between metal particles with other metal particles and molecules, and thus can be used to optimize SERS[30] and plasmon enhanced fluorescence.[35] In addition, the benefits of a silica shell in the growth of bimetallic nanorods were already demonstrated[36,37] in at least two papers. In the first paper, Au nanoparticles grown inside empty silica shells were used to seed the growth of other metals within the rod-like silica shells.[36] In ref 37, patchy silica layers were grown around AuNRs at the particles' ends or midsections. Subsequently, the noncoated regions could be overgrown by another metal. Such bimetallic AuNR-metal nanostructures have unique plasmonic properties[37,38] and catalytic activities,[39,40] both caused by unique combinations of the properties of the two metals.

Here, we report a novel approach in which we oxidatively etched monodisperse AuNRs within meso-SiO_2 shells by dissolved O_2 at the tips of the nanorods only, enabling a precise control over the aspect ratio. The oxidation speed could be varied by changing the acid concentration and/or temperature. Furthermore, we show that it is possible to overgrow the resulting AuNRs by several noble metals in the mesoporous shells. The plasmonic properties of the AuNRs-metal nanostructures were studied both experimentally and by means of FDTD calculations.

RESULTS AND DISCUSSION

AuNRs were synthesized using a modified seed-mediated method[41] and coated with a meso-SiO_2 shell.[31] For oxidative etching, the AuNRs@meso-SiO_2 in methanol was mixed with certain amounts of HCl dissolved in water and then kept at a specific increased temperature under gentle stirring (for experimental details, see Experimental Section and Supporting Information (SI)). The etching process was monitored by measuring the extinction spectra as a function of the oxidation time after quenching the reaction to room temperature by dilution in methanol. Digital photographs and transmission electron microscopy (TEM) images were also taken at different oxidation times. Figure 1a shows the extinction spectra

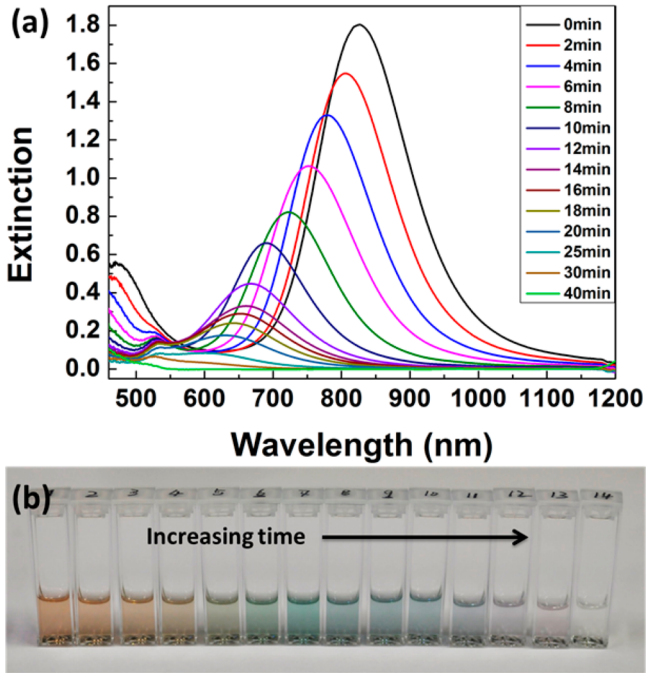

Figure 1. AuNRs were oxidatively etched by adding 0.2 mL of HCl to 10 mL of AuNRs@meso-SiO_2 methanol solution at 70 °C. (a) Extinction spectra acquired with increasing etching time. The LSPR peak blue-shifts, and the intensity decreases during oxidation due to "shortening" of the rods. (b) A digital photograph of the samples taken out with varying oxidation time for extinction spectra measurements. The shift in the LSPR peak caused a continuous color change during etching.

measured at different times after the oxidation was started by the addition of HCl solution in water. The LSPR peak of the AuNRs@meso-SiO_2 before etching was found at 827 nm with intensity 1.80 in a 1.0 cm cuvette. We estimate (see SI) a particle concentration of 2.0×10^{11} mL^{-1}. The LSPR peak was found to blue-shift, and the intensity was found to decrease during the oxidation as expected by the decreasing aspect ratio, while the TSPR peak stayed at ∼520 nm and decreased in intensity. Finally, after 40 min the AuNRs were oxidized completely, as indicated by the disappearance of any extinction peak and almost zero intensity. Figure 1b shows a digital photograph of the appearance of the dispersions of the etched-AuNRs@meso-SiO_2 at different stages. The color of the solution changed due to the varying LSPR peak. After complete oxidation of the AuNRs, the solution turned yellowish, indicating that the final oxidation product is Au(III) as Au(I) is colorless, a result that will be discussed in more detail later.

Figure 2a shows the AuNRs coated with a meso-SiO_2 shell before etching. The size parameters of initial AuNRs were 75.3 ± 9.4 nm in length (L), 17.6 ± 2.1 nm in diameter (D), and thus had an aspect ratio (AR) of 4.3 ± 0.7. Note that for the size parameters not the error in the measurement but the standard deviation (which is related to the width of the

DOI: 10.1021/acs.chemmater.5b03749
Chem. Mater. 2015, 27, 7196−7203

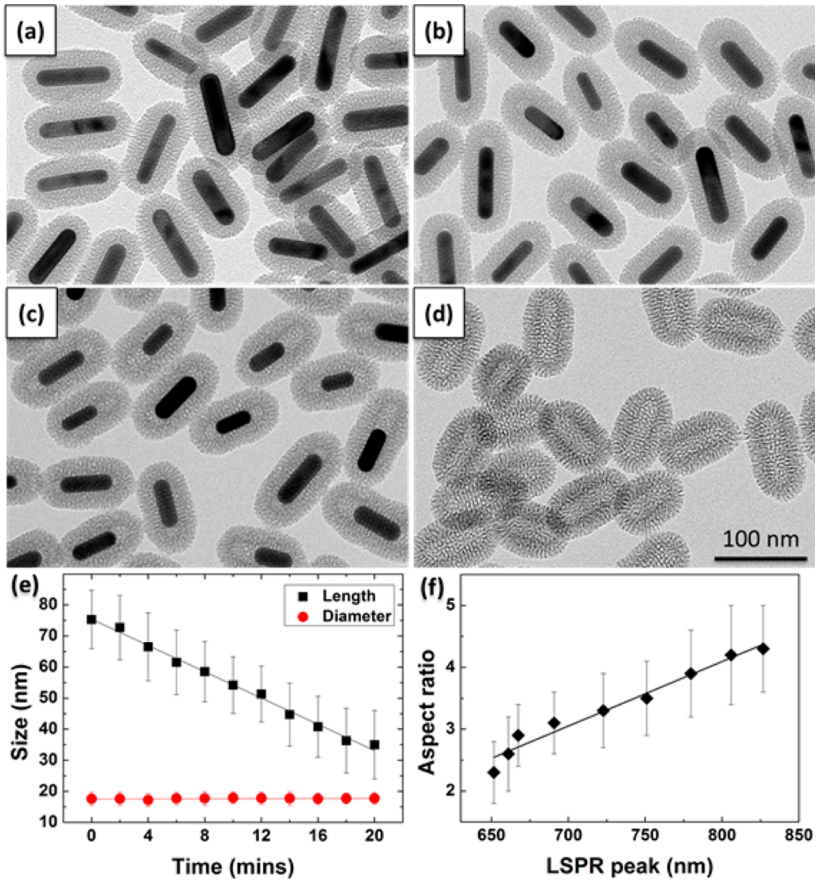

Figure 2. TEM images of AuNRs@meso-SiO_2 at different etching stages (a) t = 0 min, LSPR = 827 nm, L = (75.3 ± 9.4) nm, D = (17.6 ± 2.1) nm, and AR = 4.3 ± 0.7; (b) t = 8 min, LSPR = 723 nm, L = (58.5 ± 9.7) nm, D = (17.7 ± 2.2) nm, and AR = 3.3 ± 0.6; (c) t = 14 min, LSPR = 661 nm, L = (44.7 ± 10.1) nm, D = (17.7 ± 2.2) nm, and AR = 2.6 ± 0.6; and (d) t = 40 min, complete etching. Scale bar for a–d is shown on the bottom-right of panel d. (e) Changes of lengths and diameters of AuNRs versus etching time. With increase of the oxidation time, the length of AuNRs decreased while the diameter of AuNRs remained nearly constant. (f) The plot of aspect ratios versus LSPR peaks during etching. The line is a linear fit.

distribution or polydispersity (see SI) and was based on 200–400 particle measurements) is given. It can be seen in Figure 2e that the AuNRs were etched exclusively at the ends of nanorods (see also Figure 2b and c). After complete oxidation, only empty meso-SiO_2 shells were left due to dissolution of the AuNR cores (Figure 2d). A full set of TEM images at different etching stages are given in Figure S1. As mentioned, during the oxidation process, the diameter of nanorods remained nearly constant (Figure 2e) during the etching. Such selective etching of bare AuNRs has been reported before,[26−28] whereby oxidizing agents such as Au(III), O_2, and H_2O_2 were used. Here, we realized selective etching of the AuNRs within meso-SiO_2 shell. A plot of the aspect ratio versus the LSPR peak shows an approximately linear relationship (Figure 2f), in agreement with previous results.[1−4] In addition, the polydispersities of the etched-AuNRs in length and diameter were comparable to those of the starting AuNRs (Figure 2e), suggesting fine control of the aspect ratio of AuNRs during etching.

It was found that the oxidation speed of the AuNRs could be controlled by the HCl concentration and/or the temperature (Figure 3 and Figures S2–S4). In both cases, the initial blue-shift of the LSPR peaks was approximately linear with oxidation time. Therefore, the slope of the LSPR position with time can be used to estimate the etching speed. At fixed temperature (70 °C), the oxidation speed was found to increase with increasing

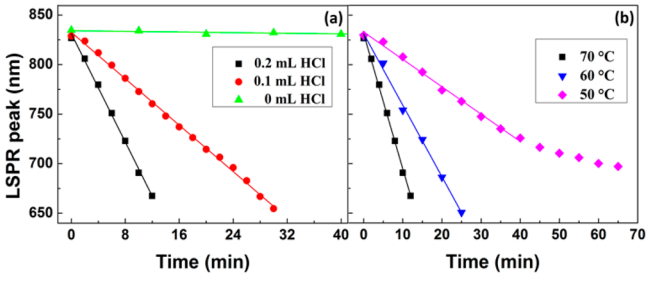

Figure 3. Etching rate of AuNRs@meso-SiO_2 could be controlled via the (a) HCl concentration and (b) temperature. The line is a linear fit. The slopes (etching rates) are <0.01 nm/min, 5.9 nm/min, and 13.7 nm/min for 0 mL of HCl, 0.1 mL of HCl, and 0.2 mL of HCl, respectively, and 7.2 nm/min and 2.8 nm/min for 60 and 50 °C, respectively.

HCl concentrations. For HCl amounts of 0 mL, 0.1 mL, and 0.2 mL, the oxidation speeds were <0.01 nm/min, 5.9 nm/min, and 13.7 nm/min, respectively. The negligible oxidation rate in the absence of HCl indicates that acidic conditions are required for oxidative etching at the conditions of our experiments. The oxidation speed could also be tuned by varying the temperature. At fixed HCl concentration (0.2 mL) but temperatures equal to 60 and 50 °C, the oxidation rates measured were 7.2 nm/min and 2.8 nm/min, respectively. Full extinction spectra

DOI: 10.1021/acs.chemmater.5b03749
Chem. Mater. 2015, 27, 7196–7203

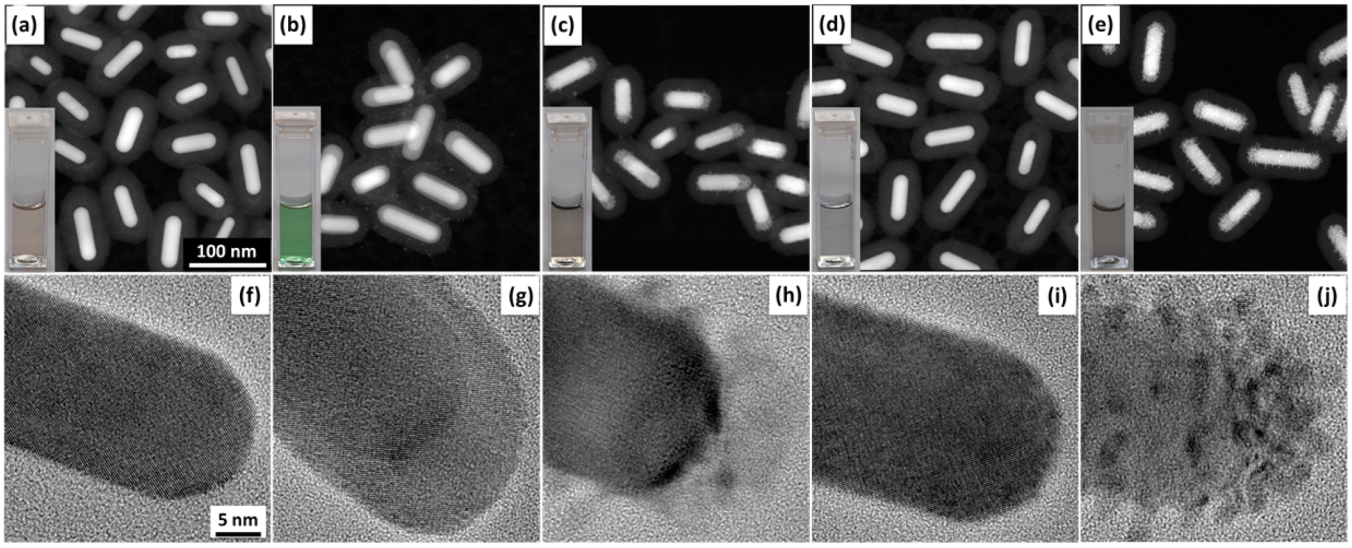

Figure 4. HAADF-STEM and HRTEM images of (a,f) etched-AuNRs@meso-SiO_2, (b,g) AuNRs-Ag@meso-SiO_2, (c,h) AuNRs-Pd@meso-SiO_2, (d,i) AuNRs-Pt-smooth@meso-SiO_2, and (e,j) AuNRs-Pt-rough@meso-SiO_2. The HRTEM images are shown at full resolution in Figure S10. The insets on the bottom-left of a−e are optical images of the samples for extinction spectra measurements.

and digital photographs are shown in Figures S2−S4. As expected (results not shown in detail), the etching speed was also found to depend on the exact details (thickness and pore volume-sizes) of the mesoporous layer. However, for similar conditions etching speeds were reproducible. For this reason, the concentrations of dissolved O_2 were not determined or controlled as also these will vary with many of the parameters used in the etching solution such as amount of water, temperature, and pH. Thus, for fine-tuning the aspect ratio of a particular dispersion of AuNRs@meso-SiO_2, it suffices to determine the initial speed and from this stop at the required aspect ratio by a temperature quench (see also below).

To investigate the oxidative reaction mechanism of the AuNRs in meso-SiO_2 shells in more detail, we performed several control experiments (Figures S5−S9). First, we determined that metallic Au(0) was oxidized to Au(III) in the following way: after the reaction was completed, the solution was mixed with a certain amount of CTAB aqueous solution. The peak that appeared around 400 nm coloring the solution a clear yellow (Figure S5, inset) was caused by the metal−ligand charge transfer absorption of $AuBr_4^-$,[26,28] which suggests that Au was present as Au(III) (Figure S5). Second, the presence of O_2 in the air above the etching solution is required for the complete dissolution of the AuNRs. When the oxidation reaction was performed under inert N_2 atmosphere, there was only minimal etching of the AuNRs. After etching for 2 h, the LSPR peak was found to blue-shift only 43 nm (Figure S6), indicating that the oxidation speed was much slower and incomplete under the N_2 atmosphere strongly suggesting that O_2 is the oxidizing agent and is replenished by dissolution from the air above the dispersion. Third, it was found that heating is not required for AuNR oxidation. At room temperature (~20 °C), the oxidation also proceeded. The reaction speed was relatively slow (<3 nm/h), but the oxidation reaction could be completed in 200 h (Figure S7). The appearance of the peak at around 400 nm again suggested that the final state was Au(III) (Figure S7, inset). Fourth, the porosity of the meso-SiO_2 shell was found to influence the oxidation speed. To illustrate this point in a dramatic way, before etching, a Stöber SiO_2 shell[42] was grown onto the AuNRs@meso-SiO_2 (total ~25 nm shell thickness after growth). The LSPR peak blue-shifted only 5 nm after etching for 2 h (Figure S8), suggesting that the accessibility for the dissolved O_2 to reach the metal surface for a "normal" Stöber SiO_2 shell without a mesoporous pore is very poor and that such a layer can effectively prevent oxidation. This result is in complete agreement with those of Matijevic who could prevent the oxidation of metallic Fe with a Stöber layer of similar thickness.[43] Finally, CTAB is not required for the oxidation of the AuNRs. Before oxidation, CTAB was removed from the meso-SiO_2 shell by calcination of the AuNRs@meso-SiO_2 particles at 500 °C in air for 6 h. The AuNRs core was partially deformed to a lower aspect ratio of 1.9 ± 0.2, and the calcined particles were redispersed in methanol for the oxidation reaction. The oxidation could still be completed, but the speed was slower than the oxidation without calcination (Figure S9), most probably by a reduction in the pore volume and/or sizes. From the results obtained, we propose the following overall reaction for the oxidative etching process:

$$4Au + 16Cl^- + 3O_2 + 12H^+ = 4AuCl_4^- + 6H_2O \quad (1)$$

Here, H^+ enhances the reduction potential of the O_2 half reaction from 0.401 to 1.229 V (vs a normal hydrogen electrode, NHE), while Cl^- acts as complexing agent, which reduces the reduction potential of Au(0)/Au(III) from 1.52 to 1.002 V (vs NHE; see SI).[24]

The etched-AuNRs@meso-SiO_2 were used for a second metal overgrowth. The etched-AuNRs core acts as a "seed" making the reduced metal salts specifically deposit on the AuNRs, with the meso-SiO_2 shell acting as "nanocontainer" which confines the shape and size of the final nanostructures. To illustrate the generality of this approach, we successfully completed the overgrowth of the noble metals (Ag, Pd, and Pt) on etched-AuNRs in a meso-SiO_2 shell. We found additionally that by varying the speed of growth both smooth layers and layers with very rough almost dendritic overlayers could be realized.

The etched-AuNRs@meso-SiO_2 particles were used for metal overgrowth by adding metal salt as precursor and ascorbic acid as reducing agent. The AuNRs-metal@meso-SiO_2

DOI: 10.1021/acs.chemmater.5b03749
Chem. Mater. 2015, 27, 7196−7203

nanostructures were investigated by high angle annular dark field scanning transmission electron microscopy (HAADF-STEM) and high-resolution transmission electron microscopy (HRTEM) imaging (Figure 4 and Figures S10 and S11). It is likely that part of the CTAB is removed from the mesopores in the silica shell so that precursor molecules can access the surface of the AuNRs. The openness of the pores likely influences the effectiveness of the overgrowth reaction. The meso-SiO_2 shell is accessible from all directions; therefore, a second metal can be grown on both the sides and the ends of the AuNRs. Because of the exclusive anisotropic etching at the ends only, there is more space at the ends of AuNR inside the SiO_2 shells, resulting in thicker metal overgrowth at the ends. Thus, the length was found to increase more than the diameter in the final AuNRs-metal structures. Figure 4a and f show the etched-AuNRs@meso-SiO_2 particles. The AuNRs are single crystals of face-centered cubic (fcc) structure, with one of the main cubic axes oriented along the length of the rod. In general, they are observed to lie on the grid either in a [110] or in a [100] orientation (Figure S10), in agreement with previous reports.[44,45] The growth behavior varied for different metals. Ag could be epitaxially grown on the AuNR surface, forming an AuNRs-Ag core−shell structure with a single crystalline structure (Figure 4g). The epitaxial growth of Ag on Au is possible due to the small lattice mismatch and the low interface energy between Au and Ag. We also found line defects in some of the AuNRs-Ag structures (Figure S11), which might arise from a too fast growth speed. For Pd growth, epitaxial growth occurred only in a few atomic layers. Thereafter, Pd nanoparticles were grown on both the sides and ends of the AuNRs (Figure 4h and Figure S10c). For Pt overgrowth, the Pt layers could be either smooth or rough, depending on the speed of growth. When the growth speed is slow, the Pt layer is smooth (Figure 4i), and the morphology is similar to that of a single AuNR. The success coating of Pt was confirmed by elemental mapping (Figure S12). When the growth speed is faster, dendritic layers were obtained (Figure 4j), and the structure is similar to the AuNRs-Pd nanostructure. The insets in Figure 4a−e show obvious color changes after metal growth: from brown to green after Ag growth and from brown to dark brown after Pd and Pt growth. The different color changes are due to the differences in the plasmonic properties after the second metal overgrowth.

To investigate the plasmonic properties of the AuNRs-metal nanostructures in more detail, we compared measured extinction spectra with FDTD calculated spectra for single composite rods with different geometries and compositions. Figure 5a shows the experimental extinction spectra of the etched-AuNRs and AuNRs-metal structures. For the LSPR of the AuNRs-Ag nanostructures, the peak blue-shifted (from 741 to 709 nm), and the peak intensity increased dramatically. The blue-shift and intensity increase arise from the higher plasmonic resonance energy and decrease in plasmonic damping of Ag compared to Au.[46] However, for the AuNRs-Pd and AuNRs-Pt-rough nanostructures, the LSPR peak red-shifted, decreased in intensity, and broadened. The red-shift is due to a slight increase in aspect ratio, whereas the intensity reduction and broadening arise from plasmon damping due to the large imaginary part of both the Pd and Pt dielectric functions.[37,38] For the AuNRs-Pt-smooth nanostructure, the LSPR did not show an obvious shift. This unchanged LSPR band is due to nearly the same aspect ratio after the Pt overgrowth. As mentioned, we performed FDTD simulations to calculate the

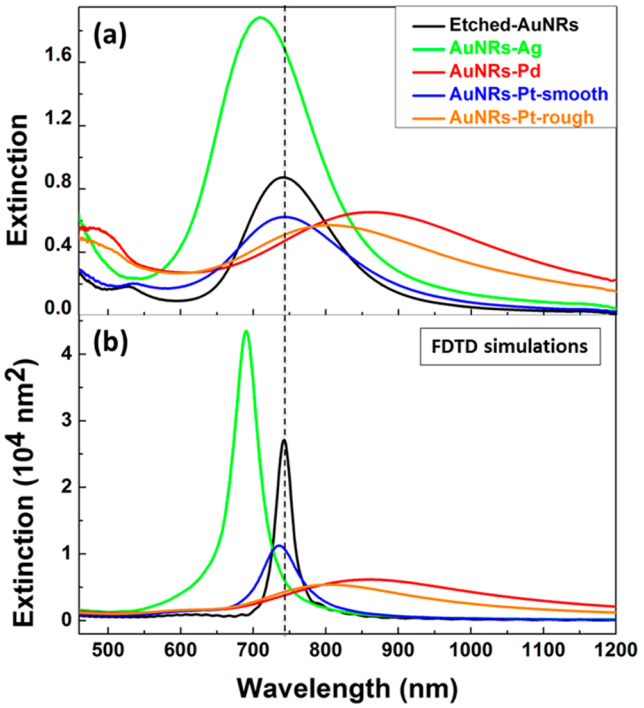

Figure 5. Experimental and simulated extinction spectra of AuNRs-metal nanostructures. (a) Experimental extinction spectra of etched-AuNRs@meso-SiO_2 (black, 70 °C, 0.2 mL of HCl in 10 mL of methanol, t = 8 min), AuNRs-Ag@meso-SiO_2 (green), AuNRs-Pd@meso-SiO_2 (red), AuNRs-Pt-smooth@meso-SiO_2 (blue), and AuNRs-Pt-rough@meso-SiO_2 (orange). (b) Extinction spectra obtained from FDTD simulations. The size parameters (L × D) were set to be the same as the ones measured from the TEM images: 58.5 nm × 17.7 nm for etched-AuNRs, 71.9 nm × 26.3 nm for AuNRs-Ag, 78.6 nm × 19.4 nm for AuNRs-Pd, 59.5 nm × 18.7 nm for AuNRs-Pt-smooth, and 70.2 nm × 20.2 nm for AuNRs-Pt-rough, respectively. Only LSPR was calculated by setting the polarization parallel to the long axis of the nanorod.

extinction cross-sections for different geometries of single AuNRs-metal nanostructures using the dielectric functions of the corresponding bulk materials (Figure 5b). We assumed a porosity of 63% in our mesoporous layer of silica[47] to which we assigned a refractive index of 1.45[48] and that the pores were filled with water solvent with a refractive index of 1.33 through a volume weighed average of the pores and silica. We obtained an effective index of refraction of 1.38, which we assumed to be valid for all wavelengths. We are aware of the fact that there is a small effect on the rod resonance frequency caused by the fact that the outer mesoporous layer encounters yet another index jump to the bulk water, but earlier work has shown this effect on the metal resonances to be quite small (only several nanometer shifts for our parameters).[49] We therefore ignored this effect in the calculations. The characteristics of the plasmonic properties after the metal overgrowth in the FDTD simulations are in good agreement with the experimental data. The only important difference is the width of the peaks, which is explained by the polydispersity of our systems which was not taken into account in the single particle calculations.

CONCLUSIONS

In summary, we have demonstrated a relatively simple approach to selectively control the dimensions of AuNRs@

DOI: 10.1021/acs.chemmater.5b03749
Chem. Mater. 2015, 27, 7196−7203

meso-SiO_2 rods after synthesis via oxidative etching. The etching speed could be precisely controlled by the HCl concentration and/or temperature but is also dependent on the mesoporous layer characteristics. Additionally, the etched AuNRs@meso-SiO_2 particles can be used as seeds for a second metal overgrowth of the etched-AuNRs in their meso-SiO_2 shells. The growth only takes place inside the mesoporous silica shell, which stabilizes the rods both mechanically, against aggregation and against deformations induced by increased temperatures, while still keeping the metal surface available for applications like catalysis and sensing such as SERS. Overgrowth was shown for the metals: Ag, Pd, and Pt, but we expect the procedure to work for other metals as well. The morphology of the additionally grown metal layers could be tuned to be both smooth and rough depending on the speed of growth. This was shown for Pt overgrowth, but preliminary results have shown these limits to be accessible for the other metals as well, and work is in progress to find the exact conditions for different metals. Depending on the intended use of these composite metal nanostructures in, e.g., plasmonics, sensing, and catalysis, the ability to also fine-tune this part of the morphology is an important extra control parameter. As expected, depending on the dielectric responses of the metals used, the plasmonic responses of the composite particles could be either increased (Ag) or decreased (Pd and Pt resulting in more dissipation). Moreover, also the catalytic properties are expected to show similarly large differences in properties depending on the reaction and metal composite as well. Finally, work is in progress to investigate whether alloy formation in the composite structures can be induced before the structures resort back to a spherical shape as the alloys of the metals used have unique properties as well and to the best of our knowledge have not yet been realized for anisotropic particles.

EXPERIMENTAL SECTION

Materials. All chemicals were used as received without further purification. Hexadecyltrimethylammonium bromide (CTAB, >98.0%) and sodium oleate (NaOL, >97.0%) were purchased from TCI America. Hydrogen tetrachloroaurate trihydrate ($HAuCl_4 \cdot 3H_2O$), sodium hydroxide (98%), and polyvinylpyrrolidone (PVP, average molecular weight 58000 g/mol, K29−32) were purchased from Acros Organics. L-Ascorbic Acid (BioXtra, ≥99%), silver nitrate ($AgNO_3$, ≥99%), sodium borohydride ($NaBH_4$, 99%), hydrochloric acid (HCl, 37 wt % in water), tetraethyl orthosilicate (TEOS, 98%), ammonium hydroxide solution (≥25 wt % in water), sodium tetrachloropalladate(II) (Na_2PdCl_4, 98%), and potassium tetrachloroplatinate(II) (K_2PtCl_4, 98%) were purchased from Sigma-Aldrich. Ultrapure water (Millipore Milli-Q grade) with resistivity of 18.2 MΩ was used in all of the experiments. All glassware for AuNR synthesis was cleaned with fresh aqua regia (HCl/HNO_3 in a 3:1 ratio by volume; *caution! Aqua regia is extremely corrosive and should be handled with extreme care!*) and rinsed with large amounts of water.

Oxidative Etching of AuNRs@meso-SiO_2. The oxidative etching of AuNRs in meso-SiO_2 shell was carried out by heating the AuNRs@meso-SiO_2 solution (10.0 mL in methanol) in a 40 mL glass vial to 70 °C in an oil bath. To start the etching, 0.20 mL HCl (37 wt % in water) was added. The cap of the glass vial was closed to prevent evaporation of HCl. With the increase of etching time, the color of the solution changed from brownish to green, blue, and finally yellowish (due to the formation of Au(III)). The amount of HCl (0.10 mL, 0 mL) or temperature (60 °C, 50 °C) was changed to control the etching speed. The oxidation process was monitored by measuring extinction spectra as a function of oxidation time in a 1.0 cm cuvette. The spectra were measured by taking samples from the etched-AuNRs@meso-SiO_2 solutions and mixing them with the same volume of methanol to rapidly cool down the temperature. The LSPR peak of the AuNRs@meso-SiO_2 before etching was at 827 nm and had an intensity of 1.80.

Metal Overgrowth on Etched-AuNRs@meso-SiO_2. The AuNRs@meso-SiO_2 solution (15.0 mL in methanol) was mixed with HCl (37 wt % in water, 0.30 mL) and etched at 70 °C for 8 min. The etching was stopped by adding large amounts of cool methanol and centrifuging at 8000 rpm for 10 min. The precipitate was redispersed into PVP aqueous solution (molecular weight, 58000 g/mol, 1.1 wt %). Then, the solution was centrifuged again and redispersed into PVP solution (1.1 wt %, 10.0 mL) as a stock solution. The metals were grown on etched-AuNRs@meso-SiO_2 using the method from ref 37 with modifications. For the growth of AuNRs-Ag, $AgNO_3$ (0.01M, 0.03 mL) was added into the etched-AuNRs@meso-SiO_2/PVP stock solution (0.6 mL), followed by the addition of ascorbic acid (0.03 M, 0.04 mL). The mixture was gently shaken for 20 min. For the growth of AuNRs-Pd, the conditions are the same as those for the growth of AuNRs-Ag except for the use of Na_2PdCl_4 (0.01M, 0.03 mL) instead of $AgNO_3$. For the growth of AuNRs-Pt-smooth, K_2PtCl_4 (0.01 M, 0.03 mL) was added into the etched-AuNRs@meso-SiO_2/PVP stock solution (0.6 mL), followed by the addition of ascorbic acid (0.03 M, 0.04 mL). The mixture was gently shaken for 5 min and left undisturbed for 4 h. For the growth of AuNRs-Pt-rough, K_2PtCl_4 (0.01 M, 0.12 mL) was added into the etched-AuNRs@meso-SiO_2/PVP stock solution (0.6 mL), followed by the addition of ascorbic acid (0.1 M, 0.24 mL). The mixture was gently shaken for 5 min and left undisturbed for 4 h. Since the growth speed is much slower for the growth of AuNRs-Pt, more metal salt and ascorbic acid were added to obtain the AuNRs-Pt-rough structure. Also the reaction time was much longer for Pt overgrowth. The resulting particles were centrifuged at 8000 rpm for 10 min and redispersed in water. The results are shown in Figures 4−5 and Figures S10−S12.

Characterization. Extinction spectra were measured using a vertex 70 FT-IR spectrometer (BRUKER) and 1.0 cm cuvettes. To measure the Au(III) with a peak at ∼400 nm, a PerkinElmer Lambda 950 spectrophotometer was used. TEM images were acquired with a Tecnai 12 microscope (FEI) operating at 120 kV. HAADF-STEM and HRTEM measurements on AuNRs-metal@meso-SiO_2 structures (Figures 4, S10, and S11) were performed using a cubed Titan microscope (FEI) with spherical aberration correction for bright-field imaging, and operating at 300 kV. A camera length of 115 mm was used to limit diffraction effects in HAADF-STEM imaging.[50] For the AuNRs-Pt-smooth@meso-SiO_2, EDX mapping was also performed. The particle sizes of etched-AuNRs were measured from TEM images, whereby 200−400 particles were measured for each sample. The mean (μ) and standard deviation (σ) of length (L), diameter (D), and aspect ratio were obtained by the following formula,

$$\sigma = \sqrt{\frac{1}{N}\sum_{i=1}^{N}(x_i - \mu)^2}, \quad \text{where } \mu = \frac{1}{N}\sum_{i=1}^{N} x_i$$

Here, x_i is the length (or diameter) of measured particles or the aspect ratio obtained by (L/D), and N is the number of particles. The results shown in the article are $\mu \pm \sigma$.

FDTD Simulations. Finite difference time domain (FDTD) is a method for solving Maxwell's equations on a discretized spatial grid in complex geometries. The FDTD simulations were carried out with commercial software (Lumerical FDTD Solutions 8.11). A total field scattered field source was used to simulate a propagating plane wave interacting with the nanostructures, with a wavelength range of 450 to 1200 nm. Only LSPR was calculated by setting the polarization parallel to the long axis of AuNRs. A three-dimensional nonuniform mesh was used, and a grid size of 0.5 nm was chosen for the AuNRs-metal nanostructures and the immediate vicinity of the structures. For the dimensions of AuNRs-metal nanostructures, the average sizes as determined from TEM were used. The shape of the AuNR core was modeled as a cylinder capped with a hemisphere at each end. For the AuNRs-Ag core−shell structure, the Ag shell was modeled by wrapping the AuNR core with a Ag layer. For the AuNRs-Pd (or AuNRs-Pt) nanostructure, a few Pd (or Pt) atomic layers were epitaxially grown on the AuNR surface. Thereafter, additional Pd (or

DOI: 10.1021/acs.chemmater.5b03749
Chem. Mater. 2015, 27, 7196−7203

Pt) deposition led to the formation of nanoparticles on both sides and ends of the AuNRs. Therefore, the model of AuNRs-Pd (or AuNRs-Pt) nanostructures consisted of an AuNR core wrapped by a 0.5 nm thick Pd (or Pt) layer and randomly distributed Pd (or Pt) nanoparticles (1−3 nm in diameter) on the outside. The dielectric functions of metals were obtained by fitting the points from the data of Palik, E. D. (Handbook of Optical Constants of Solids; Academic Press: Boston, MA, 1985). We assumed a porosity of 63% (f) in our mesoporous layer of silica[47] to which we assigned a refractive index of 1.45[48] (n_{SiO_2}) and that the pores were filled with water solvent with a refractive index of 1.33 (n_{H_2O}) through a volume weighed average of the pores and silica. We calculated an effective refractive index by

$$n_{\text{eff}} = \sqrt{n_{H_2O}^2 \cdot f + n_{SiO_2}^2 \cdot (1 - f)}$$

The obtained effective index of refraction is 1.38, which we assumed to be valid for all wavelengths.

■ ASSOCIATED CONTENT

Supporting Information

The Supporting Information is available free of charge on the ACS Publications website at DOI: 10.1021/acs.chemmater.5b03749.

More experimental details, full set of TEM images of etched-Au@meso-SiO_2, extinction spectra, TEM images and digital pictures of all control experiments, HRTEM images of AuNRs-metal nanostructures at full resolution, and EDX elemental mapping of AuNRs-Pt-smooth nanostructure (PDF)

■ AUTHOR INFORMATION

Corresponding Authors

*(T.S.D.) E-mail: dengts@pku.edu.cn.
*(A.v.B.) E-mail: A.vanBlaaderen@uu.nl.

Notes

The authors declare no competing financial interest.

■ ACKNOWLEDGMENTS

We thank Johannes D. Meeldijk and Chris Schneijdenberg for electron microscopy support, and Professor Jianfang Wang and Dr. Ruibing Jiang for help with the FDTD simulations. T.S.D. and A.v.B. acknowledge financial support from a European Research Council under the European Unions Seventh Framework Programme (FP/2007-2013)/ERC Grant Agreement no. [291667].

■ REFERENCES

(1) Chen, H. J.; Shao, L.; Li, Q.; Wang, J. F. Gold nanorods and their plasmonic properties. *Chem. Soc. Rev.* **2013**, *42*, 2679−2724.

(2) Vigderman, L.; Khanal, B. P.; Zubarev, E. R. Functional Gold Nanorods: Synthesis, Self-Assembly, and Sensing Applications. *Adv. Mater.* **2012**, *24*, 4811−4841.

(3) Halas, N. J.; Lal, S.; Chang, W.-S.; Link, S.; Nordlander, P. Plasmons in Strongly Coupled Metallic Nanostructures. *Chem. Rev.* **2011**, *111*, 3913−3961.

(4) Huang, X.; Neretina, S.; El-Sayed, M. A. Gold Nanorods: From Synthesis and Properties to Biological and Biomedical Applications. *Adv. Mater.* **2009**, *21*, 4880−4910.

(5) Sivapalan, S. T.; DeVetter, B. M.; Yang, T. K.; van Dijk, T.; Schulmerich, M. V.; Carney, P. S.; Bhargava, R.; Murphy, C. J. Off-Resonance Surface-Enhanced Raman Spectroscopy from Gold Nanorod Suspensions as a Function of Aspect Ratio: Not What We Thought. *ACS Nano* **2013**, *7*, 2099−2105.

(6) Alvarez-Puebla, R. A.; Agarwal, A.; Manna, P.; Khanal, B. P.; Aldeanueva-Potel, P.; Carbó-Argibay, E.; Pazos-Pérez, N.; Vigderman, L.; Zubarev, E. R.; Kotov, N. A.; Liz-Marzán, L. M. Gold nanorods 3D-supercrystals as surface enhanced Raman scattering spectroscopy substrates for the rapid detection of scrambled prions. *Proc. Natl. Acad. Sci. U. S. A.* **2011**, *108*, 8157−8161.

(7) Kabashin, A. V.; Evans, P.; Pastkovsky, S.; Hendren, W.; Wurtz, G. A.; Atkinson, R.; Pollard, R.; Podolskiy, V. A.; Zayats, A. V. Plasmonic nanorod metamaterials for biosensing. *Nat. Mater.* **2009**, *8*, 867−871.

(8) Gandra, N.; Portz, C.; Tian, L. M.; Tang, R.; Xu, B. G.; Achilefu, S.; Singamaneni, S. Probing Distance-Dependent Plasmon-Enhanced Near-Infrared Fluorescence Using Polyelectrolyte Multilayers as Dielectric Spacers. *Angew. Chem., Int. Ed.* **2014**, *53*, 866−870.

(9) Yuan, H. F.; Khatua, S.; Zijlstra, P.; Yorulmaz, M.; Orrit, M. Thousand-fold Enhancement of Single-Molecule Fluorescence Near a Single Gold Nanorod. *Angew. Chem., Int. Ed.* **2013**, *52*, 1217−1221.

(10) Ming, T.; Zhao, L.; Yang, Z.; Chen, H. J.; Sun, L. D.; Wang, J. F.; Yan, C. H. Strong Polarization Dependence of Plasmon-Enhanced Fluorescence on Single Gold Nanorods. *Nano Lett.* **2009**, *9*, 3896−3903.

(11) Knight, M. W.; Sobhani, H.; Nordlander, P.; Halas, N. J. Photodetection with Active Optical Antennas. *Science* **2011**, *332*, 702−704.

(12) Zijlstra, P.; Chon, J. W. M.; Gu, M. Five-dimensional optical recording mediated by surface plasmons in gold nanorods. *Nature* **2009**, *459*, 410−413.

(13) Huang, X. H.; El-Sayed, I. H.; Qian, W.; El-Sayed, M. A. Cancer cell imaging and photothermal therapy in the near-infrared region by using gold nanorods. *J. Am. Chem. Soc.* **2006**, *128*, 2115−2120.

(14) Dickerson, E. B.; Dreaden, E. C.; Huang, X. H.; El-Sayed, I. H.; Chu, H. H.; Pushpanketh, S.; McDonald, J. F.; El-Sayed, M. A. Gold nanorod assisted near-infrared plasmonic photothermal therapy (PPTT) of squamous cell carcinoma in mice. *Cancer Lett.* **2008**, *269*, 57−66.

(15) Zhang, Y.; Qian, J.; Wang, D.; Wang, Y. L.; He, S. L. Multifunctional Gold Nanorods with Ultrahigh Stability and Tunability for In Vivo Fluorescence Imaging, SERS Detection, and Photodynamic Therapy. *Angew. Chem., Int. Ed.* **2013**, *52*, 1148−1151.

(16) Jiang, Z. L.; Dong, B.; Chen, B. T.; Wang, J.; Xu, L.; Zhang, S.; Song, H. W. Multifunctional Au@mSiO2/Rhodamine B Isothiocyanate Nanocomposites: Cell Imaging, Photocontrolled Drug Release, and Photothermal Therapy for Cancer Cells. *Small* **2013**, *9*, 604−612.

(17) Boyer, D.; Tamarat, P.; Maali, A.; Lounis, B.; Orrit, M. Photothermal imaging of nanometer-sized metal particles among scatterers. *Science* **2002**, *297*, 1160−1163.

(18) Dreaden, E. C.; Alkilany, A. M.; Huang, X.; Murphy, C. J.; El-Sayed, M. A. The golden age: gold nanoparticles for biomedicine. *Chem. Soc. Rev.* **2012**, *41*, 2740−2779.

(19) Alkilany, A. M.; Murphy, C. J. Toxicity and cellular uptake of gold nanoparticles: what we have learned so far? *J. Nanopart. Res.* **2010**, *12*, 2313−2333.

(20) Huang, D. P.; Bai, X. T.; Zheng, L. Q. Ultrafast Preparation of Three-Dimensional Dendritic Gold Nanostructures in Aqueous Solution and Their Applications in Catalysis and SERS. *J. Phys. Chem. C* **2011**, *115*, 14641−14647.

(21) Nikoobakht, B.; El-Sayed, M. A. Preparation and growth mechanism of gold nanorods (NRs) using seed-mediated growth method. *Chem. Mater.* **2003**, *15*, 1957−1962.

(22) Jana, N. R.; Gearheart, L.; Murphy, C. J. Wet chemical synthesis of high aspect ratio cylindrical gold nanorods. *J. Phys. Chem. B* **2001**, *105*, 4065−4067.

(23) Jana, N. R.; Gearheart, L.; Murphy, C. J. Seed-mediated growth approach for shape-controlled synthesis of spheroidal and rod-like gold nanoparticles using a surfactant template. *Adv. Mater.* **2001**, *13*, 1389−1393.

(24) Long, R.; Zhou, S.; Wiley, B. J.; Xiong, Y. J. Oxidative etching for controlled synthesis of metal nanocrystals: atomic addition and subtraction. *Chem. Soc. Rev.* **2014**, *43*, 6288−6310.

DOI: 10.1021/acs.chemmater.5b03749
Chem. Mater. 2015, 27, 7196−7203

(25) Jana, N. R.; Gearheart, L.; Obare, S. O.; Murphy, C. J. Anisotropic chemical reactivity of gold spheroids and nanorods. *Langmuir* **2002**, *18*, 922−927.
(26) Rodríguez-Fernández, J.; Pérez-Juste, J.; Mulvaney, P.; Liz-Marzán, L. M. Spatially-directed oxidation of gold nanoparticles by Au(III)-CTAB complexes. *J. Phys. Chem. B* **2005**, *109*, 14257−14261.
(27) Tsung, C. K.; Kou, X. S.; Shi, Q. H.; Zhang, J. P.; Yeung, M. H.; Wang, J. F.; Stucky, G. D. Selective shortening of single-crystalline gold nanorods by mild oxidation. *J. Am. Chem. Soc.* **2006**, *128*, 5352−5353.
(28) Ni, W.; Kou, X.; Yang, Z.; Wang, J. F. Tailoring longitudinal surface plasmon wavelengths, scattering and absorption cross sections of gold nanorods. *ACS Nano* **2008**, *2*, 677−686.
(29) Son, M.; Lee, J.; Jang, D. J. Light-treated silica-coated gold nanorods having highly enhanced catalytic performances and reusability. *J. Mol. Catal. A: Chem.* **2014**, *385*, 38−45.
(30) Li, J. F.; Huang, Y. F.; Ding, Y.; Yang, Z. L.; Li, S. B.; Zhou, X. S.; Fan, F. R.; Zhang, W.; Zhou, Z. Y.; Wu, D. Y.; Ren, B.; Wang, Z. L.; Tian, Z. Q. Shell-isolated nanoparticle-enhanced Raman spectroscopy. *Nature* **2010**, *464*, 392−395.
(31) Gorelikov, I.; Matsuura, N. Single-step coating of mesoporous silica on cetyltrimethyl ammonium bromide-capped nanoparticles. *Nano Lett.* **2008**, *8*, 369−373.
(32) Guerrero-Martinez, A.; Perez-Juste, J.; Liz-Marzan, L. M. Recent Progress on Silica Coating of Nanoparticles and Related Nanomaterials. *Adv. Mater.* **2010**, *22*, 1182−1195.
(33) Hoffmann, F.; Cornelius, M.; Morell, J.; Fröba, M. Silica-based mesoporous organic-inorganic hybrid materials. *Angew. Chem., Int. Ed.* **2006**, *45*, 3216−3251.
(34) Slowing, I. I.; Trewyn, B. G.; Giri, S.; Lin, V. S. Y. Mesoporous silica nanoparticles for drug delivery and biosensing applications. *Adv. Funct. Mater.* **2007**, *17*, 1225−1236.
(35) Peng, B.; Zhang, Q.; Liu, X. F.; Ji, Y.; Demir, H. V.; Huan, C. H. A.; Sum, T. C.; Xiong, Q. H. Fluorophore-Doped Core-Multishell Spherical Plasmonic Nanocavities: Resonant Energy Transfer toward a Loss Compensation. *ACS Nano* **2012**, *6*, 6250−6259.
(36) Gao, C. B.; Zhang, Q.; Lu, Z. D.; Yin, Y. D. Templated Synthesis of Metal Nanorods in Silica Nanotubes. *J. Am. Chem. Soc.* **2011**, *133*, 19706−19709.
(37) Wang, F.; Cheng, S.; Bao, Z. H.; Wang, J. F. Anisotropic Overgrowth of Metal Heterostructures Induced by a Site-Selective Silica Coating. *Angew. Chem., Int. Ed.* **2013**, *52*, 10344−10348.
(38) Chen, H. J.; Wang, F.; Li, K.; Woo, K. C.; Wang, J. F.; Li, Q.; Sun, L. D.; Zhang, X. X.; Lin, H. Q.; Yan, C. H. Plasmonic Percolation: Plasmon-Manifested Dielectric-to-Metal Transition. *ACS Nano* **2012**, *6*, 7162−7171.
(39) Wang, F.; Li, C. H.; Chen, H. J.; Jiang, R. B.; Sun, L. D.; Li, Q.; Wang, J. F.; Yu, J. C.; Yan, C. H. Plasmonic Harvesting of Light Energy for Suzuki Coupling Reactions. *J. Am. Chem. Soc.* **2013**, *135*, 5588−5601.
(40) Huang, J. F.; Zhu, Y. H.; Lin, M.; Wang, Q. X.; Zhao, L.; Yang, Y.; Yao, K. X.; Han, Y. Site-Specific. Growth of Au-Pd Alloy Horns on Au Nanorods: A Platform for Highly Sensitive Monitoring of Catalytic Reactions by Surface Enhancement Raman Spectroscopy. *J. Am. Chem. Soc.* **2013**, *135*, 8552−8561.
(41) Ye, X. C.; Zheng, C.; Chen, J.; Gao, Y. Z.; Murray, C. B. Using Binary Surfactant Mixtures To Simultaneously Improve the Dimensional Tunability and Monodispersity in the Seeded Growth of Gold Nanorods. *Nano Lett.* **2013**, *13*, 765−771.
(42) Stöber, W.; Fink, A.; Bohn, E. CONTROLLED GROWTH OF MONODISPERSE SILICA SPHERES IN MICRON SIZE RANGE. *J. Colloid Interface Sci.* **1968**, *26*, 62−69.
(43) Ohmori, M.; Matijević, E. PREPARATION AND PROPERTIES OF UNIFORM COATED INORGANIC COLLOIDAL PARTICLES 0.8. SILICA ON IRON. *J. Colloid Interface Sci.* **1993**, *160*, 288−292.
(44) Wang, Z. L.; Mohamed, M. B.; Link, S.; El-Sayed, M. A. Crystallographic facets and shapes of gold nanorods of different aspect ratios. *Surf. Sci.* **1999**, *440*, L809−L814.
(45) Goris, B.; Bals, S.; Van den Broek, W.; Carbó-Argibay, E.; Gómez-Graña, S.; Liz-Marzán, L. M.; Van Tendeloo, G. Atomic-scale determination of surface facets in gold nanorods. *Nat. Mater.* **2012**, *11*, 930−935.
(46) Rycenga, M.; Cobley, C. M.; Zeng, J.; Li, W. Y.; Moran, C. H.; Zhang, Q.; Qin, D.; Xia, Y. N. Controlling the Synthesis and Assembly of Silver Nanostructures for Plasmonic Applications. *Chem. Rev.* **2011**, *111*, 3669−3712.
(47) Grün, M.; Unger, K. K.; Matsumoto, A.; Tsutsumi, K. Novel pathways for the preparation of mesoporous MCM-41 materials: control of porosity and morphology. *Microporous Mesoporous Mater.* **1999**, *27*, 207−216.
(48) Vanblaaderen, A.; Vrij, A. SYNTHESIS AND CHARACTERIZATION OF COLLOIDAL DISPERSIONS OF FLUORESCENT, MONODISPERSE SILICA SPHERES. *Langmuir* **1992**, *8*, 2921−2931.
(49) Pérez-Juste, J.; Pastoriza-Santos, I.; Liz-Marzán, L. M.; Mulvaney, P. Gold nanorods: Synthesis, characterization and applications. *Coord. Chem. Rev.* **2005**, *249*, 1870−1901.
(50) Yalcin, A. O.; G, B.; van Dijk-Moes, R. J. A.; Fan, Z.; Erdamar, A. K.; Tichelaar, F. D.; Vlugt, T. J. H.; Van Tendeloo, G.; Bals, S.; Vanmaekelbergh, D.; Zandbergen, H. W.; van Huis, M. A. Heat-induced transformation of CdSe/CdS/ZnS core/multishell quantum dots by Zn diffusion into inner layers. *Chem. Commun.* **2015**, *51*, 3320−3323.

DOI: 10.1021/acs.chemmater.5b03749
Chem. Mater. 2015, 27, 7196−7203